Design and Evaluation of Matrix Rotor Induction Motor for High-Torque Low-Speed Applications

Carlos Madariaga, *Student Member, IEEE,* César Gallardo, *Student Member, IEEE,* Nicolás Reyes Juan A. Tapia, *Senior Member, IEEE,* Werner Jara, *Member, IEEE,* Michele Degano, *Senior Member, IEEE*

***Abstract*—This paper presents the design and evaluation of a new axial-flux low-speed and high-torque matrix-rotor induction machine. Iron wires embedded in a cupper matrix comprise the solid rotor structure. Specific design and sizing equations are provided focusing on key rotor parameters: the iron/copper ratio and iron wire diameter. The analysis was carried out through analytical equations and three-dimensional finite element simulations. Based on the proposed design guidelines, A 20 HP, 250 rpm prototype was built and evaluated for experimental validation. Good concordance was obtained between the different stages of the matrix-rotor induction machine design: the initial sizing recommendations, finite element simulations and experimental results. Moreover, the proposed machine is suitable for low-speed high-torque applications, although there is room for further optimization depending on specific application needs.**

***Index Terms*--Axial flux motors, induction motors, matrix rotor, solid rotor.**

I. Introduction

SEVERAL applications require low-speed high-torque (LSHT) operation in order to move heavy loads, such as conveyor belts and mills used in mining industry. Coupled with a gearbox or belts, permanent magnet synchronous machines (PMSMs) and induction machines (IMs) have been the most widely used machines for these applications in the last decades [1]. PMSMs exhibit a high torque density capability, at the expense of needing large amounts of rare-earth permanent magnets [2]. In turn, IMs are considered a mature technology, widely used in the industry [3], known for their high reliability [4] and relatively low cost. Since both topologies must operate coupled with a mechanical converter to reduce speed and increase torque, the reliability of the system is reduced, and overall costs increase [5]. In fact, mechanical power converters require regular maintenance due to the extremely high torque and friction during its operation, whilst efficiency is also affected.

In the search for more efficient, reliable and direct-drive capable machines, axial flux permanent machine synchronous machines (AF-PMSMs) have gained interest in recent years [6]-[7]. Their ability to adopt a high pole count allows for the possibility of direct motor-load connection, reducing space requirements and eliminating the need for mechanical converters.

However, concerns regarding rare-earth scarcity, price fluctuations, supply shortage, environmental and social impact have increased the interest in other technologies [2],[8]. Among them, axial flux induction motors (AFIM), sketched in Fig. 1(a), have proven to be a suitable alternative given they provide several advantages when compared with their radial counterparts in several applications: low inertia, compactness, short axial length, higher power density, among others [9]-[12]. Finite element (FE) modelling and analysis of different AFIM topologies with both single and multiple structures can be found in recent studies [11], [13]-[14], which underlines the potential and suitability of these machines in several applications. However, even when the AFIM may be advantageous in high-torque and low-speed applications, they have inherently high leakage flux [15]-[16], which decreases their overall performance and can trigger a significative reduction of power factor, a torque ripple increase, among other undesired effects [17]-[19].

The proposal of design improvements and new designs of

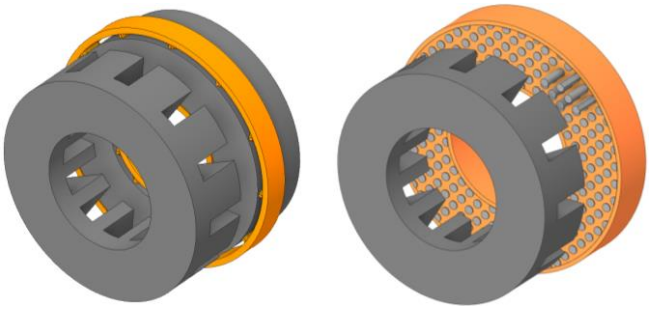

(a) (b)

Fig. 1. 3D sketch of (a) axial flux square cage induction machine and (b) axial flux matrix rotor induction machine.

This work was supported in part by the Agencia Nacional de Investigación y Desarrollo (ANID), Chile, under Grant ANIDPFCHA/Doctorado Nacional/2020-21200350, Grant ANID-PFCHA/Doctorado Nacional/2020-21200527, Project FONDECYT REGULAR 1230670 and Project VIU23P0053.

C. Madariaga, C. Gallardo, N. Reyes and J. Tapia are with the Department of Electrical Engineering, University of Concepcion, Concepcion, 4070386, Chile (e-mail: carlosmadariaga@udec.cl)

W. Jara is with the School of Electrical Engineering, Pontificia Universidad Católica de Valparaíso, Valparaiso, 2362804, Chile. (e-mail werner.jara@pucv.cl).

M. Degano and C. Gallardo are with the Power Electronics and Machines Centre, University of Nottingham, Nottingham, NG7 2RD, UK. (e-mail: michele.degano@nottingham.ac.uk)

AFIM can be found in [20]-[22], based on the stacking of partial machines, rotor yoke reduction, and adjustable airgap. In [20], the authors analyze a stack of two partial machines devised from single-stator AFIMs with squirrel cage, discussing their performance when reducing the rotor yoke: the magnetic coupling results in a higher stator current when compared to a single induction machine, which leads to high copper losses. Also, the authors provide recommendations over the operation of these magnetically coupled machines, which can be useful to further analyze multiple-stator multiple-rotor AFIMs. In [21], a novel axial flux single-rotor single-stator AFIM with adjustable airgap length is presented, whilst in [22] an improved design of single-rotor and single-stator AFIM, through the shaping of radial slot opening, is presented. These new structures allow to minimize the airgap length by solving the problem of high magnetic pull (axial forces). Consequently, the aforementioned design considerations provide the motor with higher performance ratings than it is possible with longer airgap length. Nevertheless, these machines are designed for rated speeds over 1000 rpm and a low pole count, which is significantly off the direct-drive high-torque and low-speed application niche.

An unconventional and scarcely investigated solution to high flux leakage and performance penalization is changing the structure of the rotor, adopting a solid rotor with a matrix structure. Initially introduced in [15] and later addressed in [23]-[24], this machine dealt with very promising concepts when originally proposed, i.e. to reduce the flux leakage through the arrangement of magnetic channels located in the stator core (see. Fig 1(b)). Nevertheless, designs presented in [23]-[24] did not count with experimental validation, and large-scale 3D FE analysis of several designs of this machine were not feasible by the time this machine was proposed. Therefore, its competitivity and application niche were never fully disclosed.

Previous work presenting FE evaluations of a matrix-rotor (MR) AFIM showed to be promising, as it can deliver more electromagnetic torque, and to develop lower noise than an AFIM with conventional cage rotor [24]-[25]. However, several aspects of the design, performance, manufacturing, and assembly of these machines have not been disclosed so far. Moreover, recent work only addresses theorical initial aspects of its design, but no experimental validation of an axial-flux matrix-rotor machine has been conducted to the best of the authors' knowledge.

Modern manufacturing techniques such as additive manufacturing are technology enablers for novel and non-conventional electrical machines [26]-[27], and MR-AFIM competitivity may benefit from these. Providing a detailed evaluation of this proposed design would help to decide on the suitability of MR-AFIM in LSHT applications, and to open the path for further improvement.

This paper aims to present the design guidelines of a new rare-earth free MR-AFIM for low-speed and high-torque operation. The key design parameters of the proposed topology are identified, corresponding to iron/copper ratio and iron wire diameter, and initial sizing equations are provided to fulfill rated torque and speed requirements. The analysis is carried out by means of analytical sizing equations and FE simulations. A 20 HP, 250 rpm machine prototype was manufactured for experimental validation, and it was supplied with 220 V and 380 V to evaluate the machine's performance. The remainder of the paper is organized as follows. Section II provides design considerations of both the stator and rotor structures, focusing on the parameter selection of the iron-copper matrix structure. A case study design is devised from the design guidelines of Section II and evaluated by means of 3D FE simulations in Section III. Torque, current, efficiency and power factor are assessed. In Section IV, the proposed design is prototyped, and experimental results are provided to validate the design guidelines presented in the paper. Conclusions and general remarks are summarized at the end of the paper.

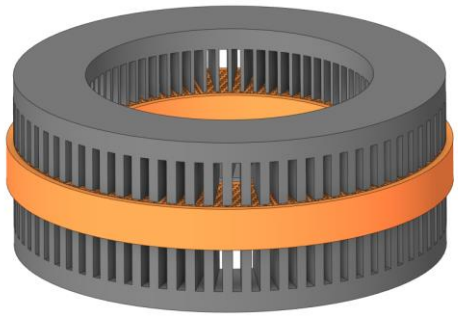

Fig. 2. Sketch of a dual-stator single-matrix-rotor induction motor.

II. Design of the Matrix-Rotor IM

AFIM can be classified according to the adopted number of stators and rotors: the simplest configuration is single-rotor and single-stator, whilst more complex configurations can have multiple rotors and multiple stators, suitable in high-power applications, since they reduce the mechanical stress in the bearings [28]. Thus, and since high-torque and low-speed are required, a double stator configuration was selected in this work, sketched in Fig. 2.

In turn, the rotor structure is proposed to be comprised of equidistant iron wires inside of a copper matrix, as depicted in Fig. 3. The wire arrangement aims to provide a high permeability in the axial direction (μ_y in the case of Fig. 3), which facilitates the conduction of magnetic flux lines from one stator to the other crossing the rotor structure. Also, it has low permeability in the other directions since the copper structure act similar to flux barriers, aiming to nullify the leakage flux. Furthermore, the copper-wire configuration and the short-circuit rings allow the free circulation of current through the rotor structure, represented as yellow lines in Fig. 3, which should diminish the equivalent resistance.

A. Analytical initial sizing

The sizing of the proposed MR-AFIM relies on pre-selecting flux density reference values in different active zones of the machine and to comply with dimension restrictions, which determines the major stator and rotor dimensions.

Considering the active parts of the magnetic circuit as both stators and the central matrix rotor, the magnetic flux crosses from one stator to the other in axial direction through the rotor

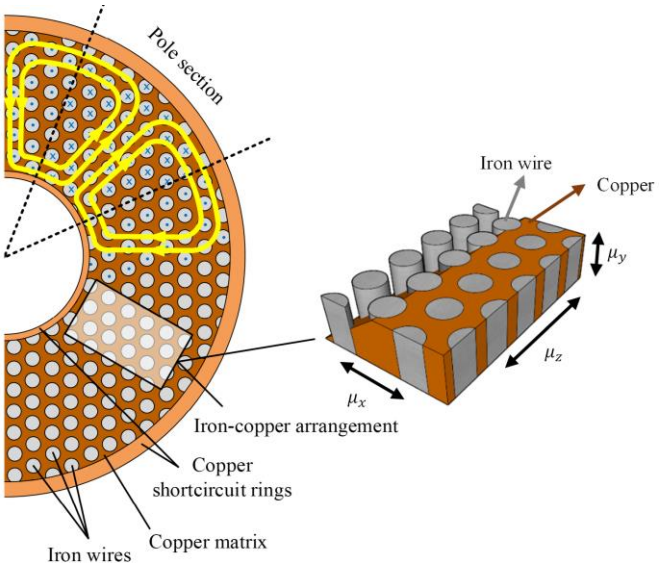

Fig. 3 Schematics of the matrix rotor structure. Magnetic flux density in the iron wires is represented as dots and crosses, and current density paths are represented as yellow lines.

structure. Taking into account the machine geometry machine, and starting from values of outer and inner diameter, the maximum magnetic flux crossing the airgap per pole ($\hat{\phi}_{\delta\text{pole}}$) can be simplified to [29]:

$$\hat{\phi}_{\delta\text{pole}} = \hat{B}_\delta \left(\frac{{D_o}^2 - {D_i}^2}{4p} \right), \tag{1}$$

where $\hat{B}_\delta$ is the maximum value of airgap flux density, and p is the number of pole pairs of the machine, which are selected depending on the objective speed and available supply frequency. Since a direct drive is pursued, frequency should range between 50Hz and 60Hz depending on the implementation location.

The maximum magnetic flux traveling through the stator teeth ($\hat{\phi}_{\text{ts,pole}}$) and stator yoke ($\hat{\phi}_{\text{ys,pole}}$) is estimated with [29]:

$$\hat{\phi}_{ts\ \text{pole}} = \frac{1}{\pi p} \hat{B}_t \left[\pi \left(\frac{{D_o}^2 - {D_i}^2}{4} \right) - \left(\frac{D_o - D_i}{2} \right) b_s Q_s \right], \tag{2}$$

$$\hat{\phi}_{\text{ys,pole}} = 2\hat{B}_{\text{ys}} \left(\frac{D_o - D_i}{2} \right) h_{\text{ys}}, \tag{3}$$

where $\hat{B}_t$ and $\hat{B}_{\text{ys}}$ are the maximum flux density values on the teeth and stator yoke respectively, b_s is the slot width, Q_s is the stator slot count and h_{ys} is the stator yoke height.

In turn, to evaluate the rotor magnetic flux ($\hat{\phi}_{\text{rotor,pole}}$), the total cross-sectional area of the iron wires of a pole section of the rotor must be considered:

$$\hat{\phi}_{\text{rotor,pole}} = \hat{B}_{\text{rotor}} \left(\frac{{D_o}^2 - {D_i}^2}{4p} \right) \cdot k_{\text{matrix}} \tag{4}$$

where k_{matrix} is the proportion between the total cross-section area of iron wires and the total pole section area. In turn, k_{matrix} depends on the ratio of iron wire diameter (D_{fe}) and the distance between adjacent iron wires (d_{fe}):

$$k_{\text{matrix}} = \frac{\pi}{2\sqrt{3}} \left(\frac{D_{\text{fe}}}{d_{\text{fe}}} \right)^2 \tag{5}$$

In order to restrain rotor saturation and the consequent rotor flux leakage, it is recommended that iron channels have a flux density value similar than that of the stator teeth. Therefore, from (2) and (4), it is suggested that:

$$k_{\text{matrix}} \approx 1 - \frac{b_s Q_s}{\pi \frac{(D_o + D_i)}{2}} \tag{6}$$

From (1)-(4) and considering the conservation of magnetic flux in the magnetic circuit, flux density values in the different parts of the machine can be initially selected to propose a first design. As a starting point, teeth and airgap magnetic load reference values can be found in the literature [29]-[30] or respond to specific application requirements. Since the airgap length significantly influences the magnetomotive-force requirements of the magnetic circuit, the Carter factor can be useful to determine an analytical equivalent airgap [30]:

$$\delta_{\text{e}} = k_c \delta \tag{7}$$

Considering standard rectangular slots, depicted in Fig. 4, and following Ostovic's Carter factor formulation [30], k_c is given by:

$$k_{\text{c}} = \begin{cases} \dfrac{\tau_s}{\tau_s - \gamma\delta} & \text{, if } b_{\text{oef}} < \tau_s \\ \dfrac{1}{1-\beta} & \text{, if } b_{\text{oef}} > \tau_s \end{cases}, \tag{8}$$

where τ_s is the slot pitch and b_{oef} is the effective slot opening, which depends on the geometric factors β and γ as per

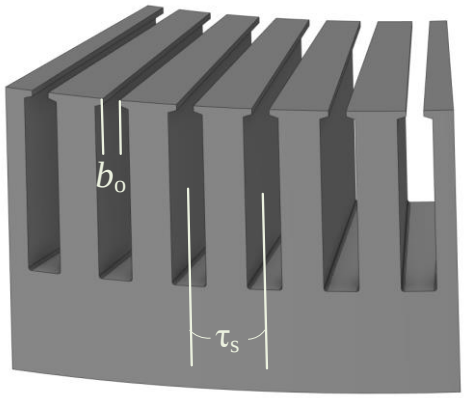

Fig. 4. Rectangular stator slots of the MR-AFIM. The slot pitch and slot opening are highlighted.

This article has been accepted for publication in IEEE Transactions on Energy Conversion. This is the author's version which has not been fully edited and content may change prior to final publication. Citation information: DOI 10.1109/TEC.2024.3426480

$$b_{\text{oef}} = \frac{\gamma\delta}{\beta} \tag{9}$$

$$\beta = \frac{\left(1 - \frac{b_o}{2\delta} - \sqrt{1 + \left(\frac{b_o}{2\delta}\right)^2}\right)^2}{2\left(1 + \left[\frac{b_o}{2\delta} + \sqrt{1 + \left(\frac{b_o}{2\delta}\right)^2}\right]^2\right)} \tag{10}$$

$$\gamma = \frac{4}{\pi}\left[\frac{b_o}{2\delta}\tan^{-1}\left(\frac{b_o}{2\delta}\right) - \ln\sqrt{1 + \left(\frac{b_o}{2\delta}\right)^2}\right] \tag{11}$$

Stator slot width and stator yoke height, as well as the minimum k_{matrix} can be therefore determined from the above procedure. In turn, slot height (h_{s}) can be initially estimated following an approach that restrains tangential stress and aims for an objective current density, as suggested in [29]. In addition, the rotor height can be initially sized from the selected stator current density value: if similar thermal stress of the rotor and stator current paths are desired, then the rotor current density should be close to that of the stator copper. This translates into the rotor height being a function of stator current density (J_{s}) and rotor current density (J_{r}):

$$h_{\text{rotor}} = \frac{J_{\text{s}}}{J_{\text{r}}} \cdot \frac{4 b_{\text{s}} h_{\text{s}} N Q_{\text{s}} N_{\text{l}} k_{\text{fill}} \cos\phi}{p(D_{\text{o}} - D_{\text{i}})(1 - k_{\text{matrix}})} \tag{12}$$

where N_{l} is the number of layers of stator windings, k_{fill} is the stator fill factor, and $\cos\phi$ is the estimated power factor.

Winding turns are defined from the supply voltage, winding factor and airgap magnetic flux per pole estimated in (1)

$$N = \frac{\xi V_{\text{ph}}}{\pi\sqrt{2} f k_{\text{w1}} \hat{\phi}_{\delta\text{pole}}}, \tag{13}$$

where V_{ph} is the phase voltage of the machine, f is the supply frequency, ξ is the ratio between the induced voltage and input phase voltage, and k_{w1} is the main component winding factor, given by:

$$k_{w1} = k_{s1} k_{d1} k_{p1}, \tag{14}$$

with k_{s1}, k_{d1}, and k_{p1} being the pitch factor, distribution factor and slot opening factor, respectively.

In summary, the pre-sizing of the MRIM starts with specific dimension restrictions and objective operating speed, from which the inner and outer diameters, pole count and stator slot count can be obtained. Considering established flux density values, the magnetic flux per pole can be obtained by means of (2), which is equal to the flux traveling through the stator slots and stator yoke (3). Then, established tooth density flux values configure the maximum slot width and minimum stator yoke. Objective torque, maximum tangential stress and maximum current density recommendations are used to calculate stator height, rotor height, whilst winding turns are calculated from the available supply voltage. Finally, it is recommended to adopt the minimum feasible airgap, and a copper-iron ratio given by (6) in order to the rotor iron wires to have a flux density value similar to that of the stator teeth.

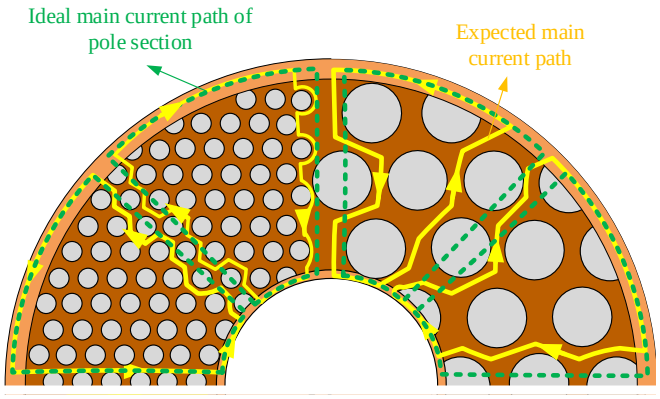

Fig. 5. Sketch of the expected main current path depending on the rotor iron wire diameter. On the left, the expected main current path is very close to the ideal, whilst on the right it may be noted that current paths should differ from the ideal, hence diminishing the proper usage of flux density.

B. Considerations on the iron wire diameter

One of the key design aspects of the MR-AFIM is the copper-iron matrix that comprises the rotor structure. As stated in (5), the proportion between iron and copper is relevant since it affects the saturation of the iron channels. In addition, and considering a fixed k_{matrix}, different iron wire diameter values can be adopted. Theoretically, iron wire diameter should affect the establishment of current paths in the rotor structure, hence impacting on the torque generation. Since iron has a significantly lower conductivity than copper, iron wires behave as high-resistance paths. Consequently, rotor currents will mostly circulate through the copper structure, and iron wires will behave as obstacles to the ideal current paths, as depicted in Fig. 5. If larger iron wire diameter values are considered, actual current paths will differ to a further extent from the ideal paths. This causes several areas of the rotor ferromagnetic material to not be enclosed by circulating currents if larger iron wire diameters are adopted. In these zones, flux density does not contribute to torque generation, decreasing the machine electromagnetic performance.

Therefore, smaller iron wire diameter is recommended, in order to allow free circulation of rotor currents and a better usage of the magnetic flux that crosses the rotor structure. Nevertheless, manufacturing limitations and tolerances can be faced when very small iron wire diameters are desired, which should be considered as a trade-off in the design stage.

C. Data of machine case study.

Following the above procedure and starting from the requirements of Table I, a 72-slot 24-pole machine is proposed as a case study to achieve a rotor speed close to 250 rpm directly connected to a 50 Hz supply. Double-layer distributed-winding (DL-DW) was considered because of its advantages in terms of heat dissipation and low spatial harmonic of the winding magneto-motive force (MMF) distribution. The main data of

TABLE I. INITIAL PARAMETERS/REQUIREMENTS OF A MRIM STUDY CASE

Symbol	Variable	Value	Unit
D_o	Outer diameter	600	mm
D_i	Inner diameter	400	mm
N_m	Rotor synchronous speed	250	RPM
δ	Airgap length	2	mm
D_{fe}	Iron wire diameter	3	mm
P_r	Rated power	20	HP
J_s	Stator current density	3	A/mm2

TABLE II. MAIN DATA OF THE CASE STUDY MACHINE

Symbol	Variable	Value	Unit
Q_s	Number of slots per stator	72	-
p	Number of pole pairs	12	-
l_r	Rotor axial length	67.5	mm
h_{ys}	Height of stator yoke	38	mm
k_{matrix}	Rotor iron/copper proportion	0.45	-
b_s	Slot width	12	mm
h_s	Slot height	60	mm

the machine are presented in Table II.

III. FINITE ELEMENT EVALUATION

A. Model and evaluation of suggested rotor parameters

To evaluate the performance of the proposed MR-AFIM design, the FE method was used by means of a commercial software package (ANSYS Electronics Desktop). Considering the geometry of the machine, a 3D model was devised, which is shown in Fig. 6(a). The FE model mesh was created with high density in the airgap and the rotor iron/cupper matrix, as depicted in Fig. 6(b), as the major interest in this paper focuses on the rotor structure and its electromagnetic response. Also, the periodicity of the machine was taken advantage of to reduce the computational burden: after mesh refinement, the two-pole section was mapped with 1.2 million tetrahedra, requiring 60GB of RAM to compute using a direct solver. When using a high-end desktop 32-core computer and parallelization, the evaluation of stable-state performance indicators required 15 hours per each slip value.

Two main suggestions were addressed in Section IIA and IIB to design an AF-MRIM: i) to minimize the iron wire diameter so as to allow the free circulation of current paths in the rotor copper section; and ii) that the value of k_{matrix} comply with (6). In Fig. 7, the comparison of the current paths created when considering two different iron wire diameters (7 and 20 mm) is presented. From Fig. 7(a), it can be noted that adopting a lower iron wire diameter makes the current to form paths that are closer to the theoretically ideal (see Fig. 5). Furthermore, these current paths are configured so that most of the iron wire diameters are correctly enclosed by perpendicular current: current paths are mostly radial in the iron/copper structure and tangential in the short-circuit rings. This translates into a higher torque capacity: the rotor with 7 mm iron wires develops 23% higher mean torque.

In turn, Fig. 8 shows the relative maximum torque and efficiency of the proposed AF-MRIM for different values of k_{matrix}, obtained from FEA. 16 slip values were evaluated to obtain the stable-state mean torque and efficiency in several speed operation points, from which the maximum values were extracted. A fixed iron wire diameter and rotor height (see

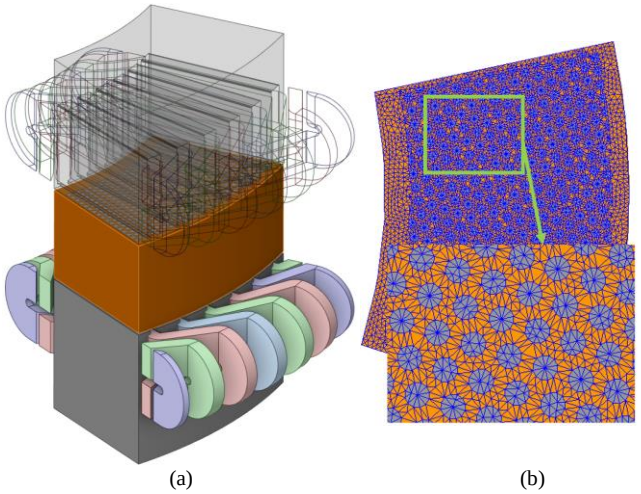

(a) (b)

Fig. 6. 3D FE model used for the evaluation of an AF-MRIM; (a) a two-pole section of the machine is modeled to take advantage of the machine periodicity; (b) a dense mesh is considered in the rotor iron/copper structure, which comprises the uniqueness of the MRIM design.

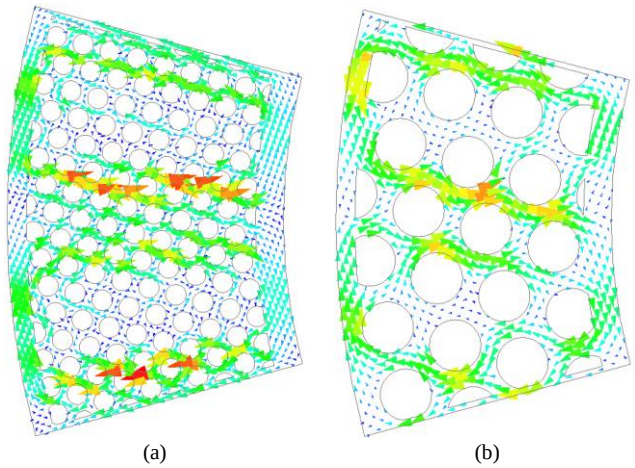

(a) (b)

Fig. 7. Comparison of the current density distribution in the cross-sectional area of the matrix rotor considering the same k_{matrix} but different iron wire diameter. (a) Iron wires have a diameter of 7 mm; (b) Iron wires have a diameter of 20 mm.

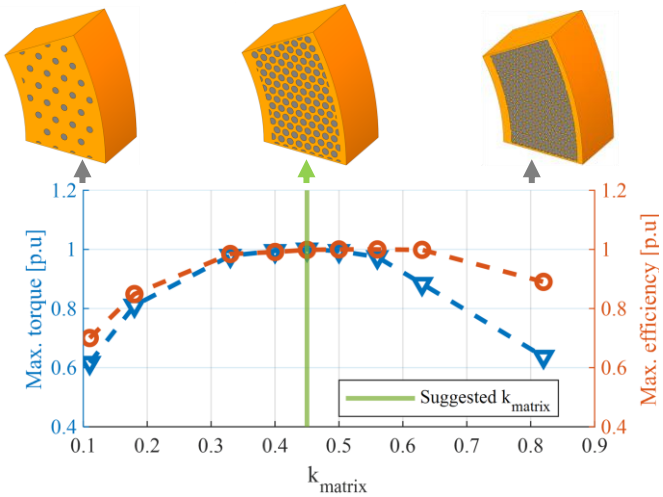

Fig. 8. Relative torque and efficiency of the proposed AF-MRIM as a function of k_{matrix}. The suggested value (6) is presented as a vertical green line. A visual representation of three values of k_{matrix} is shown at the top of the figure: two extreme values (0.1 and 0.8) and the suggested one (0.45).

Table I and II) were considered so as to isolate the effect of varying k_{matrix}. The suggested value of k_{matrix}, which is 0.45 considering the geometry of the case study machine, is highlighted as a green vertical line. Also, 1 p.u represents the maximum torque and maximum efficiency that were found for the entire simulation set. From Fig. 8, it can be noted that extreme values of k_{matrix} penalize the torque and efficiency of the machine, and the best performance is obtained in the vicinity of the suggested value (0.45). Also, values of k_{matrix} higher than the suggested in (6) can seem tempting since a lower magnetic load will be developed in the iron wires, and the torque capacity is not significantly penalized. However, in the case of further increasing k_{matrix}, the current density of the rotor copper structure will increase as well, which translates into higher thermal losses. On the other hand, adopting a smaller k_{matrix} decreases the rotor current density, but the saturation of the iron channels gets severe, hence diminishing the leakage-restriction effect and penalizing the torque capacity of the machine. It is therefore recommended to adopt a k_{matrix} close to (6) depending on the manufacturing availability, in order to have a good torque and efficiency response of the AF-MRIM. A sensitivity analysis of other main geometric parameters shows well-known tendencies for axial flux machines and can be found in [24].

B. Electromagnetic performance

In Fig. 9, relevant performance indicators of the proposed AF-MRIM are presented, obtained by means of 3D FE simulations. Average torque, efficiency, stator current and power factor were obtained for 16 different slip values in motor mode operation. Since low-voltage industrial direct-drive is desired, two line-to-line voltage values were applied: 220V@50Hz and 380V@50Hz, which are usually available in several implementation locations depending on the winding connection. From Fig. 9(a), it can be noted that the objective torque is obtained at 380V, 2% slip, considering 580 Nm at 245 rpm, which accounts for an output power of 20 HP. Furthermore, the maximum torque developed by the machine is 920 Nm when fed with 380V, which drops to approximately to 310 Nm when changing to 220V. Maximum torque is approximately two times the starting torque, and a very narrow stable speed range is obtained in both cases, approximately [235 250] rpm. Hence, the machine develops a very robust speed response: slight variations of the load torque will not be translated into significant speed variations. From Fig. 9(b), it is noticeable that the stator line current ranges from 34 to 88A for the 220V connection, and from 64 to 150A for the 380V connection. The starting current is at double the current in low slip operation, which, opposed to traditional cage IMs (starting current being 5-7 times the rated), facilitates the implementation of the MRIM in direct-drive applications. From Fig. 9(c) and Fig. 9(d), it can be seen that the efficiency and the power factor are quite similar for both 220V and 380V. Efficiency is higher than 60% in most of the linear zone for slip values within [1% 10%], and maximum efficiency of ~75% is obtained at ~3% slip. Considering the topology, high pole count, low speed and direct drive operation, efficiency values are suitable. In turn, maximum power factor is around 0.5 for both voltage inputs, although a slight decrease is observed when the voltage rises from 220 to 380V. This occurs because the rotor iron wires are more saturated in the 380V operation, hence decreasing the flux leakage nullifying effect of the iron-copper matrix.

C. Comparison with conventional machines in LSHT applications

The proposed MRIM was compared with two well-known radial topologies, radial-flux squirrel cage induction machine (SCIM) and radial-flux surface mounted permanent magnet machine (PMSM). Multi-objective genetic algorithm optimization was considered, aiming to maximize mean torque, efficiency and power factor of the SCIM and the PMSM. The evolution of design samples of both machines is presented in Fig. 10. The comparison was carried out considering a supply line-to-line voltage of ~380V at 50 Hz, an objective speed of ~250 rpm, and taking into account a current density restriction

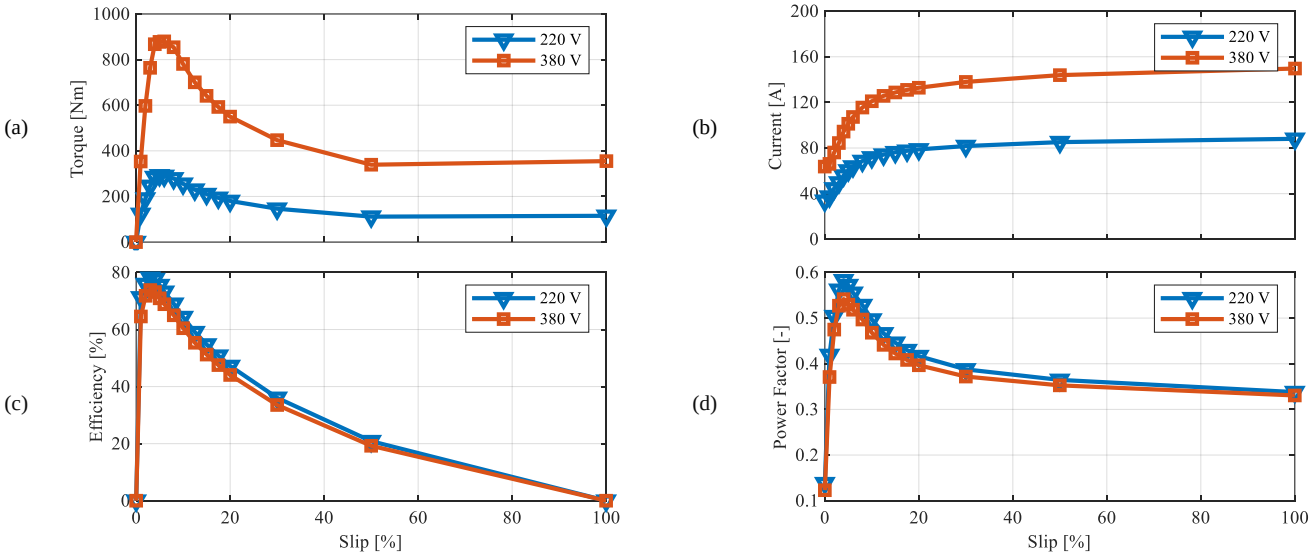

Fig. 9. Electromagnetic behavior of the MR-AFIM under the whole slip spectrum for different voltage levels. (a) Electromagnetic torque. (b) RMS value of stator line current. (c) Efficiency. (d) Power factor.

This article has been accepted for publication in IEEE Transactions on Energy Conversion. This is the author's version which has not been fully edited and content may change prior to final publication. Citation information: DOI 10.1109/TEC.2024.3426480

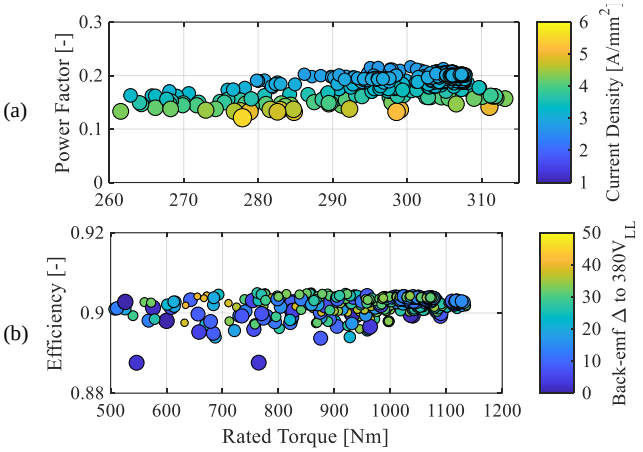

Fig. 10. Optimization evolution results. (a) Rated torque, power factor and stator current density of each SCIM specimen are presented. (b) Rated torque, efficiency and distance to the desired back-EMF of each PMSM specimen are presented.

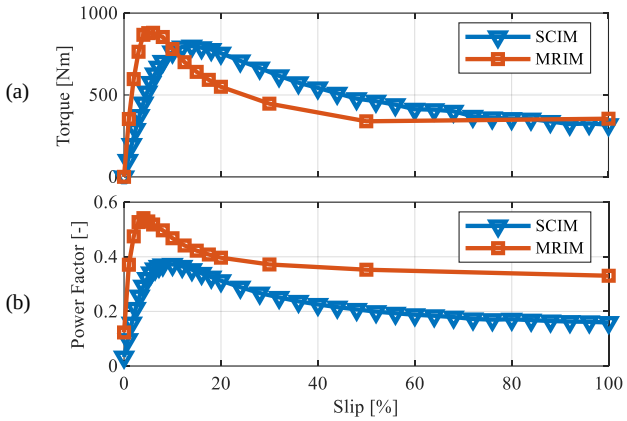

Fig. 11. Comparison of relevant performance indicators of the proposed unoptimized MRIM and an optimized SCIM. (a) Torque-slip characteristic. (b) power factor-slip characteristic.

of ~3 A/mm^2, similar to those of the MR-AFIM. Additionally, overall volume of the machines was kept close to that of the original MR-AFIM. The performance of the optimized SCIM and PMSM when compared with the proposed MRIM is presented in Table III.

It may be noted that the unoptimized MR-AFIM design develops higher mean torque, slightly higher efficiency, and double the power factor of the SCIM at the same current density; this underlines the design advantages of the matrix rotor in high-pole-count low-speed applications linked to a flux leakage decrease. As can be noted from Fig. 10, the power factor developed by the SCIM is notably low, which stems from the proposed multi-objective optimization, high pole count and stringent volume and current density limitations. From results of a specifically devised optimization problem, aiming only maximum power factor and mean torque, rated power factor of 0.35 can be reached, which is still lower than the proposed MRIM. If the same problem is solved for a 12-pole SCIM, higher power factor and performance ratings could be obtained.

In turn, the optimized PMSM has the edge on the performance chart, providing a consistent higher mean torque, efficiency, and power factor. The inclusion of the PMSM in this comparison is for raw performance comparison only since it lies outside the boundaries of this paper: the PMSM relies on rare-earth NdFeB magnets, it does not have the capacity of self-starting, and a specific drive is required for a proper operation of the machine, which makes the adoption of this topology in direct-drive operation unfeasible.

It can be appreciated that the performance of the unoptimized MRIM is significantly better than that of the optimized SCIM but relatively far from what a PMSM can offer when coupled with a proper control scheme. Nevertheless, there is room for further improvement of the MR-AFIM: performance refinement could be done by means of a progressive simplification of the FE model, subject to a multi-objective optimization problem. A 2D multi-slice modeling of the machine could be devised, simplifying the rotor response to a representative isotropic material with an equivalent BH curve, aiming to maximize efficiency, power factor and torque capacity at low-slip operation. Nonetheless, this is out of the scope of the paper, and thorough validation should be showcased in order to prove this refinement methodology.

In Fig. 11, a comparison of the torque- and power factor-slip characteristics between the optimized SCIM and the proposed MRIM (unoptimized) is presented. The torque and power factor differences between both machines is noticeable in the entire motor-operation slip range, with the MRIM having at least 20 more points. In this sense, it is clear that the MRIM has a significant advantage over SCIM, showcasing the superiority of the matrix rotor in this operation scenario.

TABLE III. PERFORMANCE OF OPTIMIZED SCIM AND PMSM IN COMPARISON WITH THE PROPOSED MRIM

Symbol	Variable	Base MRIM	Opt SCIM	Opt PMSM
J_r	Rated current density	3 A/mm^2	3 A/mm^2	3 A/mm^2
$T_{m,rated}$	Rated mean torque	553.2 Nm	270.1 Nm	815.4 Nm
η_r	Rated efficiency	71.8%	68.6 %	90.4 %
$\cos\phi_r$	Rated power factor	0.48	0.23	0.86

IV. EXPERIMENTAL VALIDATION

A. Manufacturing

Based on the dimensions and design considerations explained above, a 20 HP prototype was manufactured, as schematized in the exploded view shown in Fig 12. The stator core is made of M400-50A, and electrical steel (1020) was used for the iron wires. The mechanical design of the motor included

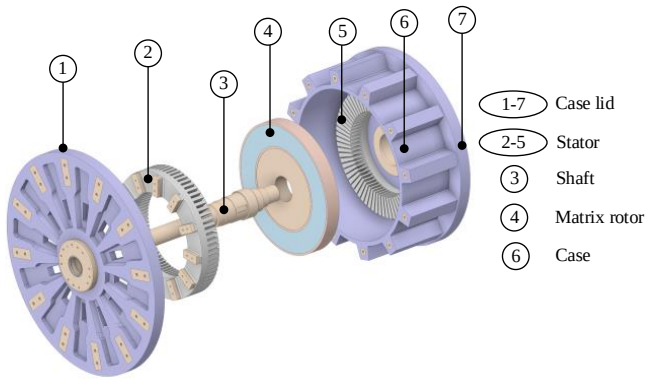

Fig. 12. Exploded view of the AF-MRIM. The mechanical parts of the machine are listed for better understanding.

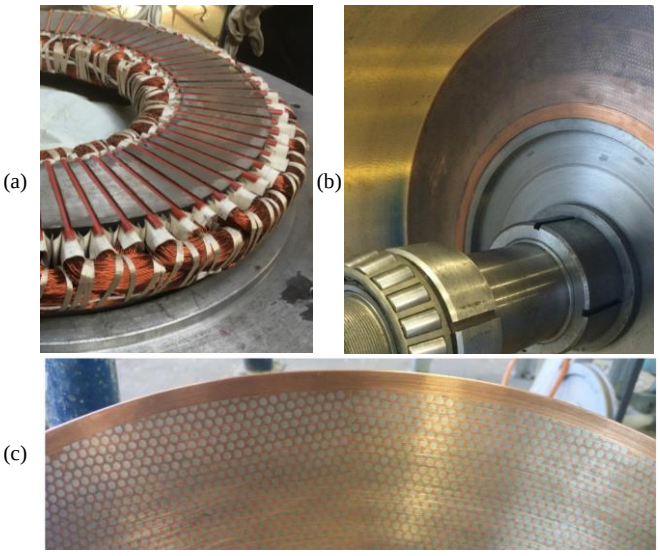

Fig. 13. Manufactured parts of the machine. (a) Stator and winding. (b) Rotor and shaft. (c) Anisotropic matrix rotor.

the shaft and case design to withstand fatigue and high cyclic loads. The shaft was made of SAE4340, whilst aluminum alloy C355 was selected for the case due to its high-performance characteristics, including low weight, high thermal conductivity, and good mechanical resistance. Aluminum parts incorporate steel inserts to increase structural rigidity. In turn, tapered rolling bearings support the shaft while keeping the rotor in place. The rotor manufacturing consisted of four steps, similar to the technique used for construction of NbTi superconductors. The first step was the packaging the Fe-Cu assembly: hexagonal copper rods and hexagonal copper tubes filled with low-carbon steel wires were joined together to form a copper cylinder. The second step considers isostatic pressing of the assembly, prior stretching of the assembly to improve cohesion between the copper hexagons. The process included heating to 400° C and isostatic pressing at 150 MPa helium. The third step considers heating the Fe-Cu assembly to 800° C, and pressure stretching at a slow speed and an area reduction ratio of 3.3. The initial diameter of the stretched cylinder was 278 mm. Finally, the pressure-drawn bar was machined flat on two sides and cut into several equal pieces. These pieces were welded side by side with silver alloy solder. The resulting rotor and stators, following the dimensions of Table I and II, are shown in Fig. 13.

B. Experimental setup

A picture of the test bench identifying its main parts is shown in Fig. 14. This consists of three main parts: the dynamometer, the control and monitoring units and the AF-MRIM prototype.

The dynamometer is composed of an 8-pole 45-kW induction machine (IM) connected to an ABB ACS800-11 55-kW converter that operates in regenerative mode to simulate the mechanical load effect. The control and monitoring units include a Danfoss FC 302 55-kW converter connected to the AF-MRIM in order to control the operation of the motor. Load tests were carried out using U/f control at different voltage levels and constant frequency. The voltage and current

Fig. 14. Test bench and equipment used to operate the AF-MRIM prototype.

measurements are performed with Yokogawa voltage probes and Tektronix A621 current sensors connected to a Yokogawa WT1806E power analyzer. The torque and speed measurements are estimated by ABB converter, and these signals are processed in the power analyzer. On the other hand, a Yokogawa DL850 oscilloscope and Yokogawa voltage probes were used to register the voltage on the windings.

C. Experimental results

In Fig. 15, relevant performance indicators of the proposed AF-MRIM are compared with the experimental measured data. Average torque, efficiency, stator current and power factor were obtained using the experimental test bench presented in Fig. 14. The machine was operated under 3% of slip to avoid surpassing thermal restrictions of the machine. A Fluke TiS55 infrared thermographic camera was used to register temperature readings at 2.0% slip operation, obtaining temperatures lower than 75 °C in the end-winding area and rotor inner surface, considered as an operation of feasible continuous operation. As it can be seen from Fig. 15, a good agreement was obtained between experimental and FE results: the built machine was able to deliver up to 600 Nm at 242 rpm in direct-drive 380V, 50 Hz operation, reaching the objective torque and output power. A very precise estimation was observed for the 220V case, since the saturation of the machine was low for the considered speed range. In the case of the 380V, a slightly higher estimation error was found in the slip-torque and slip-current characteristics, since a higher saturation was obtained and leakage-inductance precomputations can differ considering manufacturing and assembly tolerances. Nevertheless, the finite element model was able to correctly estimate the machine performance and to validate the proof of concept.

V. Conclusions

In this paper, the design guidelines and evaluation of a low-speed and high-torque matrix-rotor induction machine are presented. The proposed topology is a rare-earth free axial-flux machine with a solid rotor structure comprised by iron wires embedded in a cupper matrix. Along with classical axial-flux stator parameters, key rotor parameters were identified: the iron/copper ratio and iron wire diameter. These have a significant impact on the efficiency, power factor, torque capacity of the proposed machine. Small iron wire diameter, dependent on the available manufacturing techniques, allow for

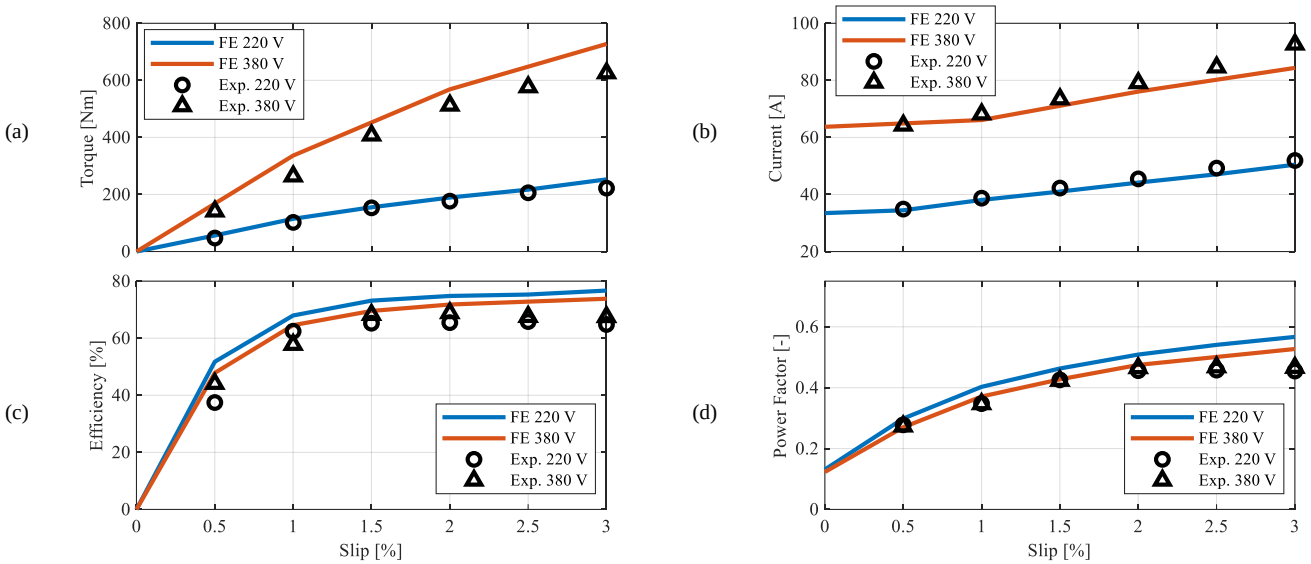

Fig. 15. FE and experimental measured data comparison of the MR-AFIM for different voltage levels. (a) Electromagnetic torque. (b) Phase RMS current. (c) Efficiency. (d) Power factor.

improved efficiency and torque capacity. In turn, there are iron/cupper ratio values that allow for higher torque, power factor and efficiency, and are dependent on stator parameters.

This analysis, carried out through analytical sizing equations and detailed three-dimensional FE simulations, was validated by means of building and evaluating a 20 HP prototype. FE simulations allowed to preliminary verify the main assumptions defined in the proposed sizing equations, which focused on the key rotor parameters. In turn, good concordance was obtained between FE simulations and experimental results, which evaluated the machine's performance in direct-drive operation. The resulting machine was able to deliver the objective torque at moderate efficiency, although within the expected from FE estimations and low-speed operation.

Nevertheless, it was found that the proposed matrix-rotor IM is suitable for LSHT applications, although there is room for further improvement. Starting from speed and torque requirements, an initial MR-AFIM design can be devised by considering the guidelines provided in this paper, which can be later optimized depending on specific application needs.

VI. References

[1] S. Evon; R. Schiferl, “Direct-drive induction motors: using an induction motor as an alternative to a motor with reducer,” IEEE Ind. Appl. Mag., vol. 11, no. 4, pp. 45-51, Jul.-Aug. 2005.

[2] G. Artetxe, D. Caballero, B. Prieto, M. Martinez-Iturralde, I. Elosegui, “Eliminating rare earth permanent magnets on low-speed high-torque machines: A performance and cost comparison of synchronous reluctance machines, ferrite permanent magnet-synchronous reluctance machines and permanent magnet synchronous machines for a direct drive elevator system,” IET Electr. Power Appl. vol. 15, no. 3, pp. 370–378, Mar. 2021.

[3] M. Al-Badri and P. Pillay, "Modified efficiency estimation tool for three-phase induction motors," IEEE Trans. Energy Convers., vol. 38, no. 2, pp. 771-779, June 2023.

[4] D. G. Dunn, L. Reamer, D. Bogh and W. R. Finley, "Introduction to IEEE 841-2020 for severe duty squirrel cage induction motors—up to and including 370 kw (500 hp): improving motor reliability, maintainability, and energy efficiency," IEEE Ind. Appl. Mag., vol. 29, no. 1, pp. 12-21, Jan.-Feb. 2023.

[5] T. M. Jahns, "The expanding role of PM machines in direct-drive applications," International Conference on Electrical Machines and Systems, Beijing, China, 2011, pp. 1-6.

[6] W. Jara, P. Lindh, J. A. Tapia, I. Petrov, A. -K. Repo and J. Pyrhönen, "Rotor eddy-current losses reduction in an axial flux permanent-magnet machine," IEEE Trans. Ind. Electron., vol. 63, no. 8, pp. 4729-4737, Aug. 2016.

[7] S. Xie, S. Cai, Y. Zuo, L. Cao, J. Zhu, A. Li, Y. Yan, C. H. T. Lee, "A new hybrid concentrated-winding concept with improved power factor for permanent magnet vernier machine," IEEE Trans. Ind. Electron., vol. 70, no. 11, pp. 11109-11120, Nov. 2023.

[8] V. Fedida, R. Qu and D. Li, "A new direct-drive induction flux modulation motor," 2020 International Conference on Electrical Machines (ICEM), Gothenburg, Sweden, 2020, pp. 375-381.

[9] M. Mirzaei, "Computational modeling of an axial airgap induction motor with a solid rotor," IEEE Trans. Magn., vol. 58, no. 6, pp. 1-9, Jun. 2022.

[10] Z. Cao, A. Mahmoudi, S. Kahourzade, W. L. Soong and J. R. Summers, "A comparative study of axial-flux versus radial-flux induction machines," 2020 IEEE International Conference on Power Electronics, Drives and Energy Systems (PEDES), Jaipur, India, 2020, pp. 1-6.

[11] M. A. Tapia; A. E. Hoffer; J. A. Tapia; R. R. Wallace, "Simulation and analysis of an axial flux induction machine," IEEE Lat. Am. Trans., vol. 15, no. 7, pp. 1263-1269, Jun. 2017.

[12] B. Dianati, S. Kahourzade, A. Mahmoudi, "Optimization of axial-flux induction motors for the application of electric vehicles considering driving cycles", IEEE Trans. Energy Convers., vol. 35, no. 3, pp. 1522-1533, Sep. 2020.

[13] D. K. Banchhor; A. Dhabale, "Design, modeling, and analysis of dual rotor axial flux induction motor," 2018 IEEE International Conference on Power Electronics, Drives and Energy Systems (PEDES), Chennai, India, 2018, pp. 1-6.

[14] F. Keskin; I. Senol; Y. Oner; “Performance analysis of axial-flux induction motor with skewed rotor,” Energies, vol. 13, no. 19, p. 4991, Sep. 2020.

[15] M. Ito; K. Arai; N. Takahashi; H. Kiwaki; T. Seya, "Magnetically anisotropic solid rotor of an induction motor," IEEE Trans. Energy Convers., vol. 3, no. 2, pp. 427-432, Jun. 1988.

[16] M. A. Tapia; W. Jara; R.R. Wallace; J. A. Tapia, "Parameters identification of an axial flux induction machine using field equations," 2018 XIII International Conference on Electrical Machines (ICEM), Alexandroupoli, Greece, 2018, pp. 351-357.

[17] A. Cavagnino, “Accuracy enhanced algorithms for the slot leakage inductance computation of double-layer windings,” IEEE Trans. Ind. Appl., vol. 53, no. 5, pp. 4422-4430, Jun. 2017.

[18] A. Boglietti; A. Cavagnino; M. Lazzari, “Computational algorithms for induction motor equivalent circuit parameter determination-part I: resistances and leakage reactances,” IEEE Trans. Ind. Electron., vol. 58, no. 9, pp. 3723–3733, Sep. 2011.

[19] M. Bortolozzi; L. Branz; A. Tessarolo; C. Bruzzese, “Improved analytical computation of rotor rectangular slot leakage inductance in squirrel cage induction motors,” 2015 International Conference on Sustainable

Mobility Applications, Renewables and Technology, Kuwait, Kuwait, 2015, pp. 1–5.
[20] J. Igelspacher; S. Fluegel; H. G. Herzog, “Analytic examination of coupled axial-flux induction machines with reduced yoke,” 2011 1st International Electric Drives Production Conference, Nuremeberg, Germany, 2011, pp. 153–158.
[21] Z. Nasiri-Gheidari and H. Lesani, "Optimal design of adjustable air-gap, two-speed, capacitor-run, single-phase axial flux induction motors," IEEE Trans. Energy Convers., vol. 28, no. 3, pp. 543-552, Sep. 2013.
[22] B. P. B. Arthur; U. Baskaran; “Improved air-gap flux in axial flux induction machine through shaping of radial slot opening,” Sādhanā, vol. 45, no. 134, May. 2020.
[23] Y. Kawase, T. Yamaguchi, T. Tsuji, K. Tanaka, N. Minoshima and T. Hattori, "Magnetic Field Analysis of Matrix-Rotor Induction Motor Using Parallel Computing System," IEEE Trans. Mag., vol. 47, no. 5, pp. 1062-1065, May. 2011
[24] C. Madariaga, J. Tapia, N. Reyes, W. Jara and M. Degano, "Influence of constructive parameters on the performance of an axial-flux induction machine with solid and magnetically anisotropic rotor," 2021 IEEE Energy Conversion Congress and Exposition (ECCE), Vancouver, BC, Canada, pp. 4037-4044, 2021.
[25] N. Reyes; M. A. Tapia; J. A. Tapia; W. Jara; A. E. Hoffer, "Multiphysical design of an axial induction motor with an anisotropic rotor," 2018 IEEE International Conference on Automation/XXIII Congress of the Chilean Association of Automatic Control (ICA-ACCA), Concepcion, pp. 1-7, 2018.
[26] F. Wu and A. M. EL-Refaie, "Toward additively manufactured electrical machines: opportunities and challenges," IEEE Trans. Ind. Appl., vol. 56, no. 2, pp. 1306-1320, Jul. 2020.
[27] R. Wrobel and B. Mecrow, "A comprehensive review of additive manufacturing in construction of electrical machines," IEEE Trans. Energy Convers., vol. 35, no. 2, pp. 1054-1064, Jun. 2020.
[28] R. Huang, Z. Song, H. Zhao and C. Liu, "Overview of Axial-Flux Machines and Modeling Methods," IEEE Trans. Transp. Electrific., vol. 8, no. 2, pp. 2118-2132, Jun. 2022.
[29] J. Pryhönen, T. Jokinen and V. Hrabovcová, “Design of rotating electrical machines,” Chichester, West Sussex: John Wiley & Sons, 2014.
[30] J. A. Tapia, J. Pyrhonen, J. Puranen, P. Lindh and S. Nyman, "Optimal Design of Large Permanent Magnet Synchronous Generators," IEEE Trans. Magn., vol. 49, no. 1, pp. 642-650, Jan. 2013.
[31] W. E. Jara Montecinos, Axial Flux Permanent Magnet MachinesDevelopment of Optimal Design Strategies, Acta Universitatis Lappeenrantaensis, 2016.

VII. BIOGRAPHIES

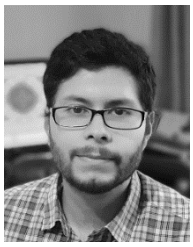

CARLOS MADARIAGA (S’16) received the B.Sc and M.Sc degrees in electrical engineering from the Pontificia Universidad Católica de Valparaíso, Chile, in 2019 and 2020 respectively. Currently, he is pursuing the Ph.D. degree at the University of Concepcion, Chile. He was granted a scholarship from the National Research Development Agency in 2020 to pursue his Ph.D. studies. His main interests are with the modelling, design, and optimization of high-performance electrical machines.

CESAR GALLARDO (S’22) received the B.Sc. degree in electrical engineering from the Central University "Marta Abreu" of Las Villas, Cuba, in 2016. He is currently pursuing the Ph.D. degree with the University of Concepción, Chile. He was granted a scholarship to pursue his Ph.D. studies from the Agencia Nacional de Investigación y Desarrollo, in 2020. His research interests include modeling, design, and optimization of electrical machines.

JUAN A. TAPIA (M’01-SM’18) received the B.Sc. and M.Sc. degrees in electrical engineering from the University of Concepción, Concepción, Chile, in 1991 and 1997, respectively, and the Ph.D. degree from the University of Wisconsin, WI, Madison in 2002. From 2010 to 2014, he was a FiDiPro Fellow with the Academy of Finland, Lappeenranta University of Technology, Lappeenranta, Finland, where he conducted research on PM machines with LUT Energy. Currently, he is working as a Professor with the Department of Electrical Engineering, University of Concepción. His research interests include electrical machine design, numerical methods for electromagnetic fields, and renewable energy.

NICOLÁS REYES received his B.Sc. degree in mechanical engineering from the University of Concepción, Chile, in 2017. He actively participated in multiple research projects of the Electrical Machines Laboratory at the University of Concepción. His research interests include the thermal and structural design of electrical machines.

WERNER JARA (M’00) received the B.Sc. degree in electrical engineering from the University of Concepción, Concepción, Chile, in 2010 and the dual D.Sc. degrees from the University of Concepción, and the Lappeenranta University of Technology, Lappeenranta, Finland, in 2016. He is currently a Professor with the Department of Electrical Engineering, Pontificia Universidad Católica de Valparaíso, Valparaíso, Chile. His current research interests include the field of electrical machines and drives, particularly numerical modeling, and design of electromagnetic devices.

MICHELE DEGANO (SM’07) Master's degree in electrical engineering from the University of Trieste, Italy, in 2011, and the Ph.D. degree in industrial engineering from the University of Padova, Italy, in 2015. Between 2014 and 2016, he was a Postdoctoral Researcher at The University of Nottingham, U.K., where he joined the Power Electronics, Machines and Control (PEMC) Research Group. In 2016 he was appointed Assistant Professor in Advanced Electrical Machines, at The University of Nottingham, U.K. He was promoted Associate Professor in 2020. His main research focuses on electrical machines and drives for industrial, automotive, railway and aerospace applications, ranging from small to large power. He is currently the PEMC Director of Industrial Liaison leading research projects for the development of future hybrid electric aerospace platforms and electric transports.